

Solvent-free thermoplastic foaming for superelastic graphene monoliths

Received: 19 June 2024

Accepted: 11 June 2025

Published online: 02 July 2025

Zeshen Li^{1,2}, Xiaotong Li^{1,2}, Kai Pang¹✉, Kaiwen Li¹, Yue Gao¹, Chengqi Zhang¹, Jiahao Lu¹, Yingjun Liu¹, Zhen Xu¹✉ & Chao Gao¹✉

Graphene monoliths with high porosity inherit extraordinary properties of graphene and establish a versatile platform to integrate diverse materials for multifunctional applications. To date, many methods have been invented to prepare graphene monoliths, including freeze-drying and templating, but these predominantly rely on fluid-based process. Direct thermoplastic foaming for graphene monoliths, as seen in the polymer industry, remains undeveloped. Here, we demonstrate a direct thermoplastic foaming strategy of a graphene monolith with high elasticity and multifunctionality. The intercalation of polymers enables the thermal plasticity of graphene oxide complex solids and allows precise control of the cellular structure of the graphene monolith. The direct thermoplastic foaming method is applicable to graphene monolith bulks, 3D-printed structures, and other 2D-nanosheets monoliths. This approach provides a facile, nontoxic, rapid and low-cost route for the industrial production of monoliths comprising graphene and various nanomaterials.

Two-dimensional sheets, such as graphene, MXene and boron nitride, have emerged as fundamental building blocks for preparing macroscopic materials via assembly methods. Lightweight porous monoliths (foams, sponges or aerogels) represent a critical class of macroscopic material that inherit the extraordinary properties of 2D sheets, transforming traditional monoliths and exhibiting exciting performances^{1–5}. As a representative example of 2D sheets-based monolith, graphene monoliths (GMs) have been engineered to exhibit ultralightness⁶, highly compressible elasticity⁷, stretchability⁸, and exceptional electrical and thermal conductivity^{9–12}. These properties make GMs highly valuable for diverse applications, spanning functional polymer composites, electromagnetic shielding, oil-water separation, and thermal management^{13–17}. The developed methods for GMs have evolved to include hydrothermal method¹⁸, freeze drying^{1,19,20} and air-bubble templated method^{21–23}, mainly starting from the dispersions of graphene oxide (GO) and featuring high cost of drying, solvent toxicity and freezing structural defects in large bulks. The great application

prospects of GMs still call for reliable and facile preparation methods for industrial production.

Polymer foams are produced by direct foaming processes, reaching millions of tons every year²⁴, establishing a paradigm for producing porous monoliths. For 2D sheet solids, the strong planar attraction between the interlayers defies the gradual growth of expanding bubbles and usually leads to catastrophic fragments, or even explodes into powders, such as when treating graphite oxide with microwave irradiation^{25,26}. The prerequisite to realize the direct plastic foaming as in polymers is to turn rigid 2D sheet solids into a plastic state. Recently, the intercalation of solvents and polymers has been developed to plasticize 2D sheet solids and utilized to plastic stretching for improving crystallinity of films and fibers, precise plastic molding and hydroplastic foaming for monoliths^{27–30}. In light of enabling plasticity, the possibility to realize the direct thermoplastic foaming of graphene without solvents as polymer species needs to be explored.

¹MOE Key Laboratory of Macromolecular Synthesis and Functionalization, Department of Polymer Science and Engineering, Key Laboratory of Adsorption and Separation Materials & Technologies of Zhejiang Province, Zhejiang University, Hangzhou, PR China. ²These authors contributed equally: Zeshen Li, Xiaotong Li. ✉e-mail: pangkai2015@zju.edu.cn; zhenxu@zju.edu.cn; chaogao@zju.edu.cn

Here, a non-solvent thermoplastic foaming (TPF) method via polymer intercalation is developed for the preparation of 2D nanomaterial monoliths directly from solids. The intercalated thermoplastic polymer provides plasticity required for the expansion of the foaming agent within GO composite solid. Tuning the content of the intercalated polymer enables GO-intercalated solids to undergo a thermally induced transition from rigidity to plasticity upon exceeding a critical interlayer gallery spacing. Through adjusting the content of foaming agent and foaming temperature, the graphene monolith with precisely controlled cellular wall thickness and density was obtained. The clustering bubbles form interconnected plateau borders characteristic of 2D sheets. After annealing, the TPF-prepared graphene monolith exhibits superelasticity ($>95\%$ strain), along with excellent electrical and thermal conductivity. The TPF method is extended to prepare MXene, MMT and BN monoliths and is compatible with bulks and 3D-printing, directing a facile, nontoxic, rapid and low-cost method for industrial production of monoliths.

Results

Fabrication and evolution of TPF process

The TPF GM was fabricated by a direct thermoplastic foaming method, which involves into three steps: microsphere foaming, growth and thermal annealing (Fig. 1a). The GO solid mixture was employed as precursor, including micro-sized graphene oxide (average sheet size $\sim 10\ \mu\text{m}$, Fig. S1), expandable microsphere (transition temperature $\sim 100^\circ\text{C}$, Fig. S2) and polymer plasticizer. As a commercial foaming

agent, the physical expanded microsphere with size of $\sim 25\ \mu\text{m}$ can be easily expanded to $\sim 62\ \mu\text{m}$ by heat treatment of 100°C , exhibiting $\sim 250\%$ increase (Figure. S3). Due to the low phase transition temperature and good affinity to GO, polyethylene glycol (PEG) was selected as plasticizers to weaken the strong hydrogen bonds with GO, providing the large enough free volume for the microsphere foaming by plastic slippages of GO sheets.

In the microsphere growth process, adjacent microspheres undergo the impinging effect due to unavoidable collisions according to Young-Laplace law³¹, leading to the formation of Plateau borders (Fig. 1b), which generated the classical honeycomb-like structure as similar as the steady-state bubble clusters (Fig. 1c). The in-situ expansion of GO solid during TPF procedure was further investigated by the infrared (Supplementary Movie 1) and digital cameras (Supplementary Movie 2), revealing this process was completed in a very short time less than 1 min (Fig. 1d and Figure. S4). During this expansion, the initially spherical pores in the GO solid gradually evolve into polygonal shapes with an average size of $\sim 60\ \mu\text{m}$ (Fig. 1e). The expansion ratio of GO solid reached up to 900% in the vertical direction with nearly unchanged lateral size (Figure. S5), demonstrating that the microsphere foaming and growth processes did not disrupt the inherently continuous connection of graphene sheets. Finally, residual microspheres and PEG was etched by high-temperature annealing at 1600°C to obtain highly porous GM (Figures S6 and S7). The restoration of graphene structure was accompanied in this process, which was testified by the low $I_D/I_G \sim 0.3$ (reduced defect density) and obvious 2D peak in Raman

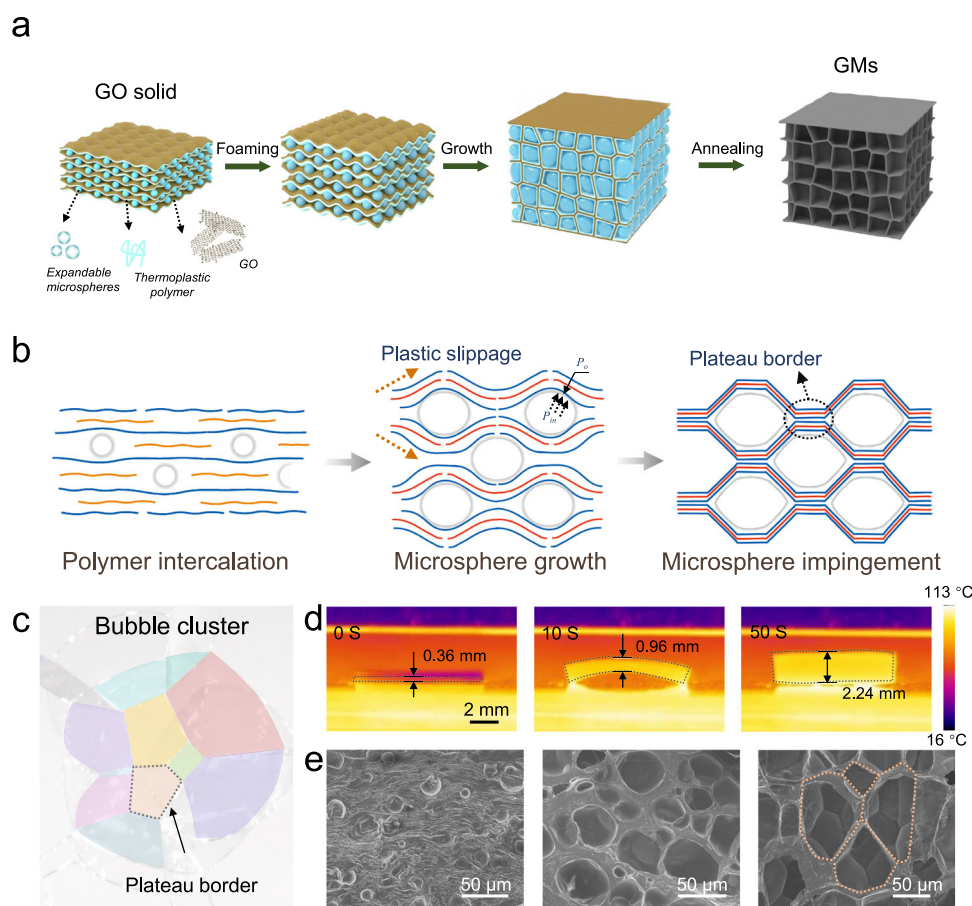


Fig. 1 | Fabrication and mechanism of thermoplastic foaming graphene monoliths (TPF GMs). **a** Schematic for TPF process. GO solid was directly transformed to monolith via three steps: microsphere foaming, growth and thermal annealing. **b** Mechanism diagram of intercalated bubble growth and impingement through polymer plasticization. **c** The structural model of multi-bubble connection.

Every bubble cell was colored with different colors to visualize the impinging effect and boundary during bubble collision. **d, e** IR snapshots of in-situ TPF process at 0 s, 10 s, 50 s and corresponding SEM images. Source data are provided as a Source Data file.

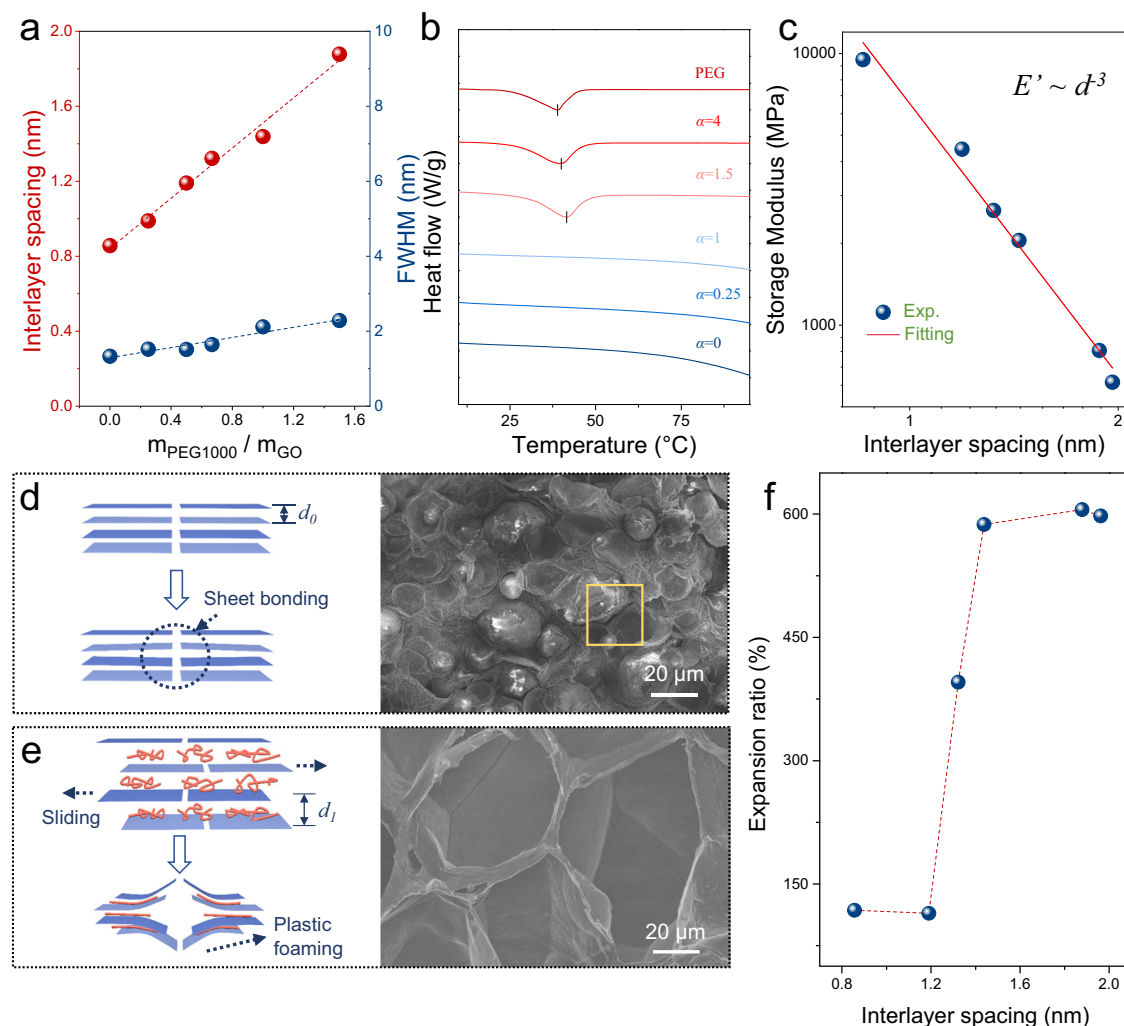


Fig. 2 | Mechanism analysis of thermoplastic foaming. **a** Corresponding interlayer spacing and FWHM of weight ratio between plasticizer and GO. **b** Peak melting temperature and its variation with different weight ratio of PEG/GO. **c** Storage modulus curves of GO composite at 100 °C with increasing interlayer spacing. The

R-squared value of the fitting line is 0.98. **d, e** Schematic of plastic foaming feasibility induced by the increased interlayer distance and corresponding morphology inspection. **f** Expansion ratio of TPF GM at 100 °C with increasing interlayer spacing. Source data are provided as a Source Data file.

spectrum^{32,33}, small peak width at half height of (002) peak in XRD pattern^{34–37}, and high C/O ratio in XPS spectrum (Figure. S8). The high-consistent Raman spectra in ten selected regions further demonstrated the structural uniformity of the annealed GM samples (Figure. S9).

Mechanism and structural control of TPF GM

The increscent interlayer spacing of GO sheets is a critical factor to enabling the fabrication of TPF GM by providing the plasticization for brittle GO solid. We revealed the interlayer spacing (d) of GO composite film and the weight ratio of PEG/GO (α) (Fig. 2a) represented a linear correlation as

$$d = 0.669\alpha + 0.842 \quad (1)$$

As depicted in Fig. 2a and Figure. S10a, the nearly unchanged full width at half maximum (FWHM) indicated the high orientation of GO even when α up to 1.5, demonstrating that the majority of GO sheets still retain flat configuration in composite film. The melting peak of PEG/GO film disappeared when α below 1, primarily due to increasing interfacial interaction and finite space^{38,39} (Fig. 2b), resulting in reduced mobility of polymer chains. However, the melting peak emerged when

α reached 1.5, indicating sufficient free interlayer space with high plasticity to enable unrestricted mobility of PEG molecules at melting temperature. We further revealed that the storage modulus (E') of GO composite exhibits an exponentially decreasing relationship with increasing interlayer spacing of GO sheets (Fig. 2c). When the experimental temperature over melting point (100 °C) of PEG molecules, the E' of GO composite ($\alpha = 0.7$) exhibited an order of magnitude lower than that of GO film (Figure S10b). However, when the temperature exceeded the decomposition point of PEG, the GO composite film became stiff and brittle, causing the GO sheets to fracture and undergo interlayer delamination due to the escape of decomposition gases (Figures S11–14). Those results demonstrated that melting PEG is a high-efficient choice to reduce the interlayer bonding and enable the high plasticity in TPF process.

The foaming capability of GO solids with different α values was further investigated to testify the critical role of plasticity in TPF. The pristine GO film effectively suppressed microsphere expansion due to strong sheet bonding, resulting in nearly unchanged microsphere size after heat treatment (Fig. 2d). In contrast, those microspheres can be easily expanded in the PEG intercalated GO film with high plasticity, achieving high porosity (Fig. 2e). The expansion ratio was defined as the final-state thickness divided by the initial thickness to determine

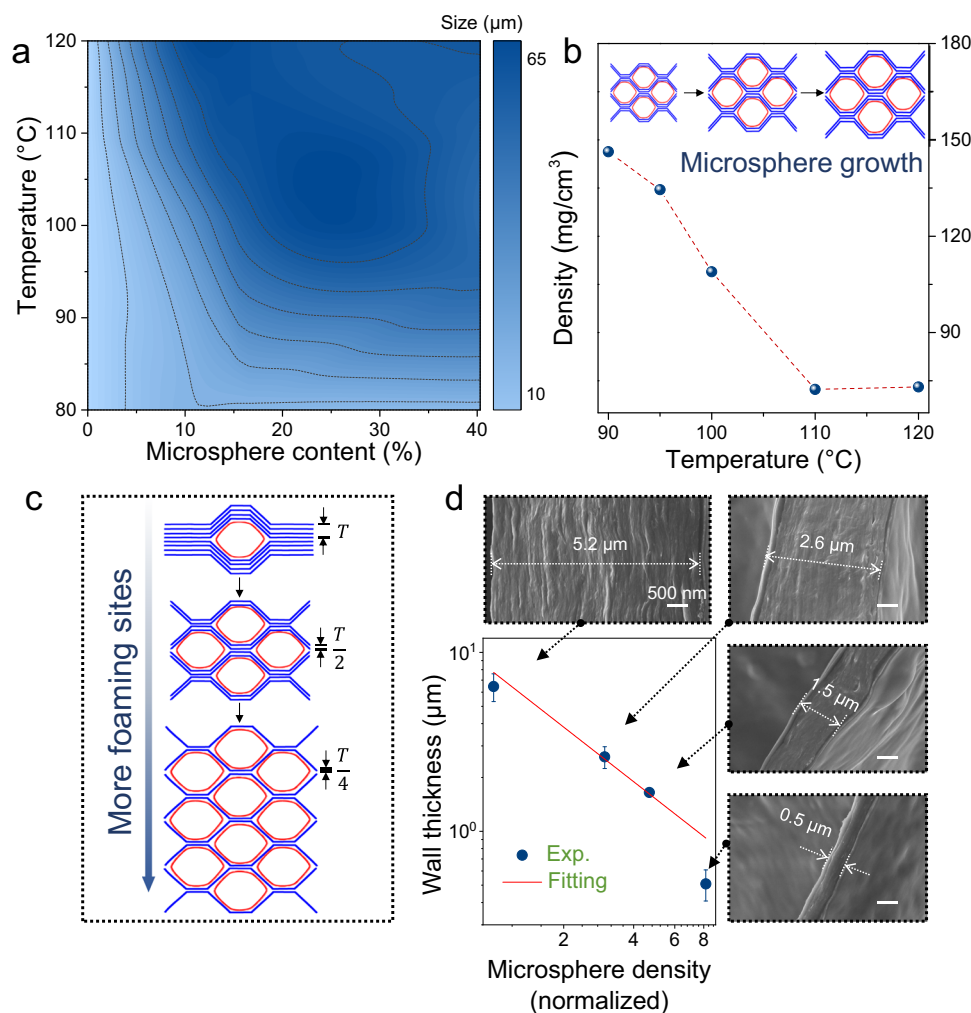


Fig. 3 | Bubbling mechanism and structural control. a A conclusive bubble size diagram with N_n and foaming temperature of the TPF process. **b** Numerical correlation of density of GO composite monoliths with temperature. **c** Diagrams of decreasing wall thickness with increasing foaming sites. **d** The tunable wall

thickness by microsphere density and their corresponding HR-SEM images. The R-squared value of the fitting line is 0.85. The x and y axes are logarithmic scales. Source data are provided as a Source Data file.

the critical interlayer spacing for the microsphere foaming. As shown in Fig. 2f and Figure. S10a, GO composite films with interlayer spacing below 1.32 nm (α below 0.7) exhibited low expansion ratio (PEG content below 40%), proving that the GO solid still mainly exhibited the brittle feature with strong binding interaction. The pore number and pore size of the monolith with α of 0.7 are obviously lower than those of the monolith with α of 1.0 (Figure. S15b, c). Therefore, the expansion ratio increased up to ~600% at the interlayer spacing of 1.44 nm ($\alpha = 1$), and reached a steady state with nearly unchanged pore size, wall thickness, pore number and density of monoliths (Figure. S15), which demonstrated that this value is the lowest PEG content to guarantee the complete foaming and growth of microspheres.

The pore size and wall thickness of the obtained monoliths were easily regulated by adjusting the foaming temperature and microsphere content, respectively (Fig. 3a). The expansion ratio of microspheres was positively correlated with temperature. As a result, the pore size of the monolith gradually increased from 49.7 to 75.1 μm as the foaming temperature increased from 80 to 100 °C, and reached the stable state at foaming temperature above 100 °C (Figure. S16). The density of the monoliths, determined by their pore size, followed the same trend with increasing foaming temperature and was regulated from 70 to 145 mg cm⁻³ (Fig. 3b). While the pore size of the

monolith was minimally affected by microsphere content, the pore number presented a positive correlation with microsphere content (Figure S17). By controlling the microsphere size, the pore size of the monoliths was tuned from 5.3 to 84.8 μm (Figure S18). Higher microsphere content led to more foaming sites, further decreasing the wall thickness of monoliths (Fig. 3c). The foaming site density (N_n) in the GO composite increased with microsphere content (M_{sphere}), following an exponential relationship of $N_n \sim M_{sphere}^{0.8}$ (Figure. S19). The wall thickness (T) can be precisely tuned from 5.2 to 0.5 μm (Fig. 3d), conforming to the exponential relationship ($T \sim N_n^{-1.08}$), which closely approaches the theoretical scaling law of $T \sim N_n^{-1}$. Moreover, fewer microsphere sites caused the lower expansion ratios of GO composite film, resulting the higher monolith density (ρ) (Figure S20). The ρ ranged from 89 to 736 mg cm⁻³, being in accordance with the exponential relation of $\rho \sim N_n^{-1.08}$. After thermal annealing at 1600 °C, the pore size and morphology showed little change with variation less than 5% (Figure S21–26 and Table S1), exhibiting the same polygonal pores with size from 9.0 to 74.6 μm. The wall thicknesses of GMs become thinner than that of GO composite monoliths due to the decomposition of PEG and microsphere (Figure. S27–29). The density of GMs decreased significantly after thermal annealing at 1600 °C, while the variation trend with temperature and microsphere density were as

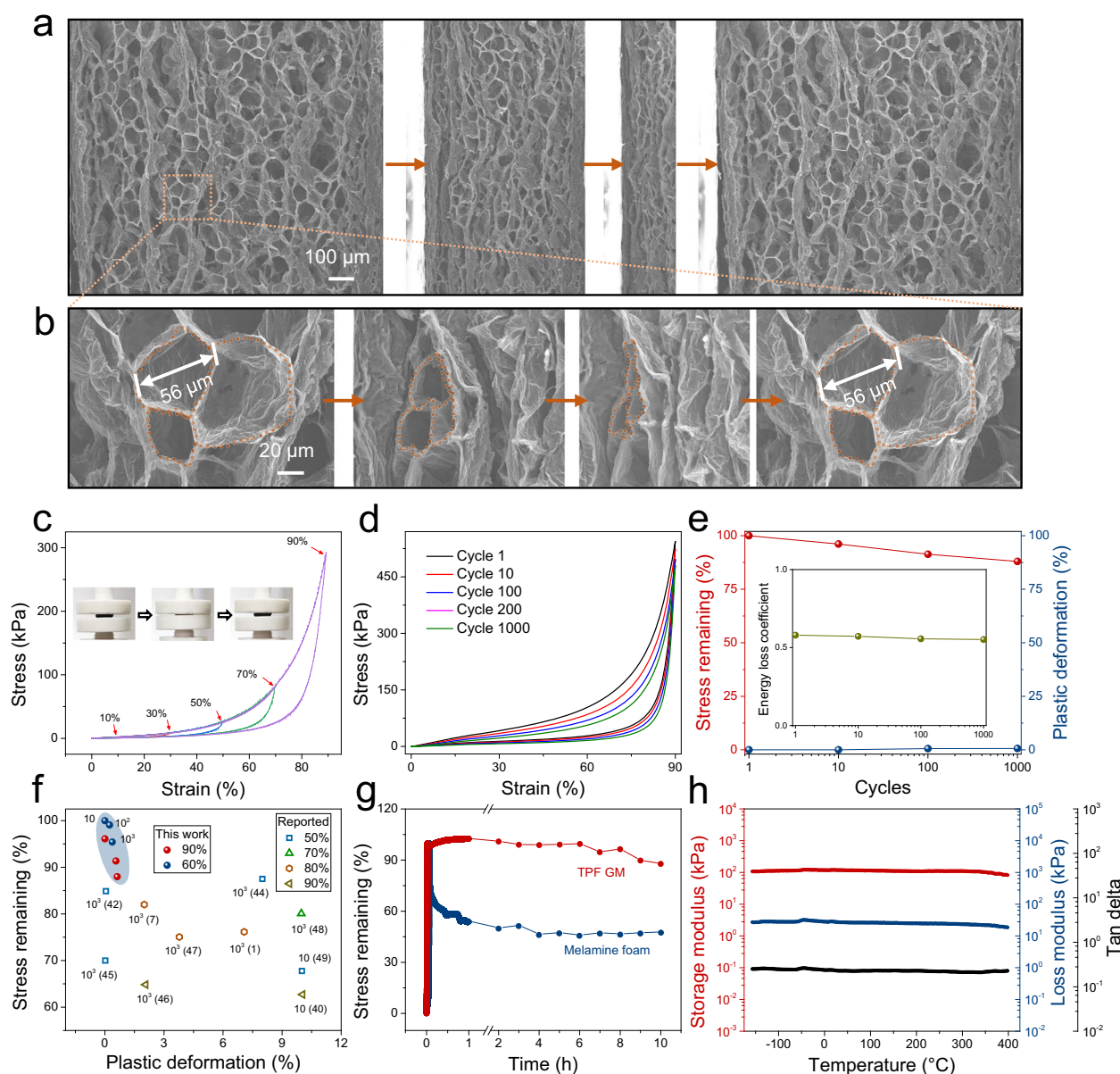


Fig. 4 | Mechanical properties of TPF GMs. **a** The in-situ SEM observation of recoverability of GM during a compressive cycle at 90% strain and **b** its microstructure evolution. **c** Strain–stress curves of GM at different compressive strains. Inset: in-situ optical images of compressive test at 90% strain. **d** Stress–strain curves of GMs under high compression strain (90%) for 10^3 cycles and **e** stress remaining, plastic deformation and energy loss coefficient during compressive cycles. **f** A

comparison chart of plastic deformation versus stress remaining during different compression cycles for TPF GMs and previously reported FD GMs. The labelled numbers correspond to the references. **g** Stress relaxation of GM and melamine foam at 95% strain for 10 h. **h** The temperature dependence of storage modulus, loss modulus and Tan delta of GMs by DMA measurements between -150 and 400 °C. Source data are provided as a Source Data file.

same as those before heat treatment. The well-established structural regulation method provides a robust foundation for the practical demands of TPF GM towards more multifunctional applications.

Mechanical performances of TPF GMs

The mechanical tests were performed to evaluate the resilience of TPF GMs, determining their practical value in engineering applications. By comparison, we found that GMs after heat treatment at 1600 °C exhibited ultralow plastic deformation (Figure S30), attributed to the complete decomposition of microsphere and restoration of graphene structure. In-situ SEM inspections (Fig. 4a) revealed that the GM structure could fully recover to the original state after 90% deformation without obvious plastic deformation. The compressive

deformation of polygon cells (Fig. 4b) was mainly divided into two stages: closing of joints and bending of walls, consistent with the behavior of typical honeycomb-like monoliths or foams. This deformation feature is further supported by the classical quadratic exponential relationship between compressive Young's modulus (E) and monolith ρ (Figure S31)^{1,20,40}. Upon unloading, the polygon cells exhibit almost no joint damage or wall cracks, with pore size remaining nearly unchanged. The TPF GM exhibited superelasticity behavior with nearly 100% recovery, exhibiting the overlapping curves at different strains from 10 to 90% (Fig. 4c). In spite of vertical direction, the GM at horizontal direction also exhibited excellent mechanical elasticity at 90% strain (Figure. S32). From longitudinal and cross-section SEM images of TPF GM, we found that the inner polygonal cell structures were

uniformly distributed and exhibited isotropic symmetry, as shown in Fast Fourier transform (FFT) images (Figure S33). After high-temperature graphitization, TPF GM featured high electrical ($8.0 \times 10^3 \text{ S m}^{-1}$) and thermal conductivity ($44.9 \text{ W m}^{-1} \text{ K}^{-1}$) in the horizontal direction, which were 32 and 13 times higher than that in vertical direction ($2.5 \times 10^2 \text{ S m}^{-1}$ and $8.2 \text{ W m}^{-1} \text{ K}^{-1}$) (Figure S34). We think those differences in electrical and thermal conductivity may be caused by the skin effect of TPF GM as arrow-marked in Figure. S33.

Figure 4d shows the fatigue curves of TPF GM at 90% compressive strain for 1000 cycles. We demonstrated TPF GM retained minimal plastic deformation ($\sim 0.6\%$), large stress remaining ($\sim 88\%$), low energy loss efficiency variation (~ 0.57) and nearly unchanged pore structure (Figure. S35), possessing great anti-fatigue performance (Fig. 4d, e). Our TPF GM elevated minimal plastic deformation and maximal remaining stress compared with previous freeze-dried (FD) monoliths^{1,7,40–47}, (Fig. 4f). TPF GM also displayed superior dynamic mechanical and environmental stability. Under long-term compression for 10 h at 95% strain, TPF GM held a higher stress remaining than polymer foam (Fig. 4g), because the elasticity of GM was energy-driven rather than entropy-driven for that of polymer foam. Owing to the structural stability of graphene at wide-temperature conditions, TPF GM exhibited excellent viscoelastic stability over a wide temperature range from -150 to 400°C while both storage and loss modulus were independent to temperature (Fig. 4h).

Structure controllability and materials universality of TPF

Benefiting from the fast and non-solvent process, a stack of large-sized GMs ($100 \text{ mm} \times 100 \text{ mm}$) can be easily fabricated (Fig. 5a), laying the foundation for the large-scale fabrication. Meanwhile, the TPF GM can be shaped adaptably to 2D and 3D structures, ranging from pre-molded shapes to curved geometry with different Gaussian curvatures (Fig. 5b), enabling special-shaped demands in applications. Furthermore, TPF GM microlattices of various shapes were fabricated by integrating with 3D printing, achieving dimensional accuracy on the order of hundreds of microns.

Apart from GM, the TPF method was also extended to other 2D sheets monoliths, such as insulating boron nitride, montmorillonite, and semiconducting MXene (Fig. 5c). Taking a $\text{Ti}_3\text{C}_2\text{T}_x$ based solid as an example, the original film can directly expand from $83 \mu\text{m}$ to 1.02 mm with a foaming ratio about 1200%, and as-prepared monolith also possessed a typical honeycomb structure (Figures S36, S37). We revealed our TPF 2D monoliths exhibited low BET surface area and little micro- and meso- pores (Figure S38), resulted by the dense micron-sized sheets were difficult to form nanoscale pores in their overlapping network^{41,48}. In contrast, the TPF GM fabricated from chemically etched 2D sheets^{22,49} exhibited high BET surface area of $271.6 \text{ m}^2/\text{g}$ with many micro- and meso- pores (Figure S38b). Furthermore, we demonstrated that those TPF 2D monoliths kept structural integrity with 100-cycle compression at high strain of 90% (Figure S39), also exhibiting excellent mechanical recoverability, which satisfied the most of practical mechanical demands. The TPF strategy provides a facile and universal processing pathway for the preparation of multi-material and multi-functional monoliths with high elasticity.

In summary, we developed a facile, non-solvent TPF method to fabricate 2D monolith directly from solids. Exemplified by GM, the intercalated polymer regulated the thermo-plasticity by enlarged interlayer spacing, meeting the premise of foaming and forming seamlessly connected 2D sheets. As-prepared GMs exhibited a hierarchically honeycomb structure with easily regulated cellular wall thickness and pores. The super-elasticity (>1000 compression-recovery cycles at 90% strain), high electrical ($8 \times 10^3 \text{ S m}^{-1}$) and thermal conductivity ($44.9 \text{ W m}^{-1} \text{ K}^{-1}$) of TPF GMs enables the multi-functionality in wide engineering applications. This TPF method can be extended to other 2D nanomaterials and is compatible with stereo structures and microlattices. This work is expected to achieve large-

scale, rapid and low-cost industrial production of novel monoliths as in the polymer industry.

Methods

Preparation of GO based composite solid

1 g of PEG and 1 g of expandable microsphere were dispersed into 10 ml of deionized water and stirred for ten minutes. The expandable microspheres are acrylic polymer microspheres with enclosing liquid alkane gas, which purchased from Nouryon (O31DU40) with particle size of $10\text{--}16 \mu\text{m}$ and foaming temperature range of $80\text{--}133^\circ\text{C}$. The prepared dilute solution was then mixed with 100 ml of GO aqueous dispersion (10 mg ml^{-1}) and stirred for thirty minutes to obtain a homogenous composite slurry with a foaming ratio of about 7. The GO based composite solids were prepared by casting obtained solutions with a thickness of 5 mm and the drying process was maintained at the ambient temperature. Different contents of PEG (0%, 33%, 40%, 50%, 60%, 70%) and expandable microsphere (0%, 5%, 10%, 15%, 30%, 50%) were prepared to control the foaming ratio.

Fabrication of GMs

For the direct TPF process, the composite solids were placed between two platens of hot press. The temperature (90°C , 100°C , 110°C , 120°C , 150°C) and time were tuned to control the foaming rate and pore size. The GM was obtained after cooling down and annealing at 1600°C ^{30,50–52}. The annealing process was performed by programmed temperature controlling. Firstly, the sample was heated to 1000°C at a rate of $5^\circ\text{C}/\text{min}$ and maintained at that temperature for 1 h. And then, the temperature was risen to 1600°C at a rate of $10^\circ\text{C}/\text{min}$ and held at this temperature for 2 h. Finally, the annealed graphene monolith was fabricated after natural cooling.

Fabrication of BN, MMT, MXene monoliths

Firstly, 10 ml of BN aqueous dispersion (10 wt%) was mixed with 50 ml of PVA solution (2 wt%) and 1 g of expandable microsphere, and then stirred for 30 min to obtain a homogenous composite slurry. The BN composite film was realized by casting method from the composite slurry, and dried at the ambient temperature. Finally, the BN composite film was directly placed on the hot plate with temperature of 100°C for 10 min, to obtained BN monoliths. By the same way, the MMT and MXene monoliths were also fabricated according to aforementioned steps.

Fabrication of 3D print TPF GM

Firstly, the composite slurry was prepared by mixing PEG and expandable microsphere with GO aqueous dispersion (20 mg ml^{-1}). The homogenous slurry was used as ink to fabricate microlattice through 3D print and then dried at the ambient temperature. Finally, the dried microlattice was directly placed on the hot plate with temperature of 100°C for 10 min, to obtain TPF GM microlattice.

Characterization

The structure and morphology of GMs were investigated by SEM and HR-SEM on Zeiss EVO-10, Hitachi S4800 and Gemini SEM 300. The microstructure and mapping of BN, MMT and $\text{Ti}_3\text{C}_2\text{T}_x$ monoliths were characterized by Hitachi SU-8010 field emission system with energy dispersive X-ray. The surface temperature profiles of in situ foaming process were detected by an infrared imager (FLIR T630sc). Electrical conductivity was measured by a standard four-probe method taken on the Keithley 2400 Source Meter. Thermal diffusivities and specific heat capacity were measured and calculated by NETZSCH LFA 467 and DSC 204HP, respectively. Nitrogen porosimetry results were measured by Micromeritics ASAP 2460. Thermogravimetric curves were obtained on NETZSCH STA 449 F3.

The peak melting temperature was measured by DSC using a TA Q20 instrument. The DSC test was performed in nitrogen with two

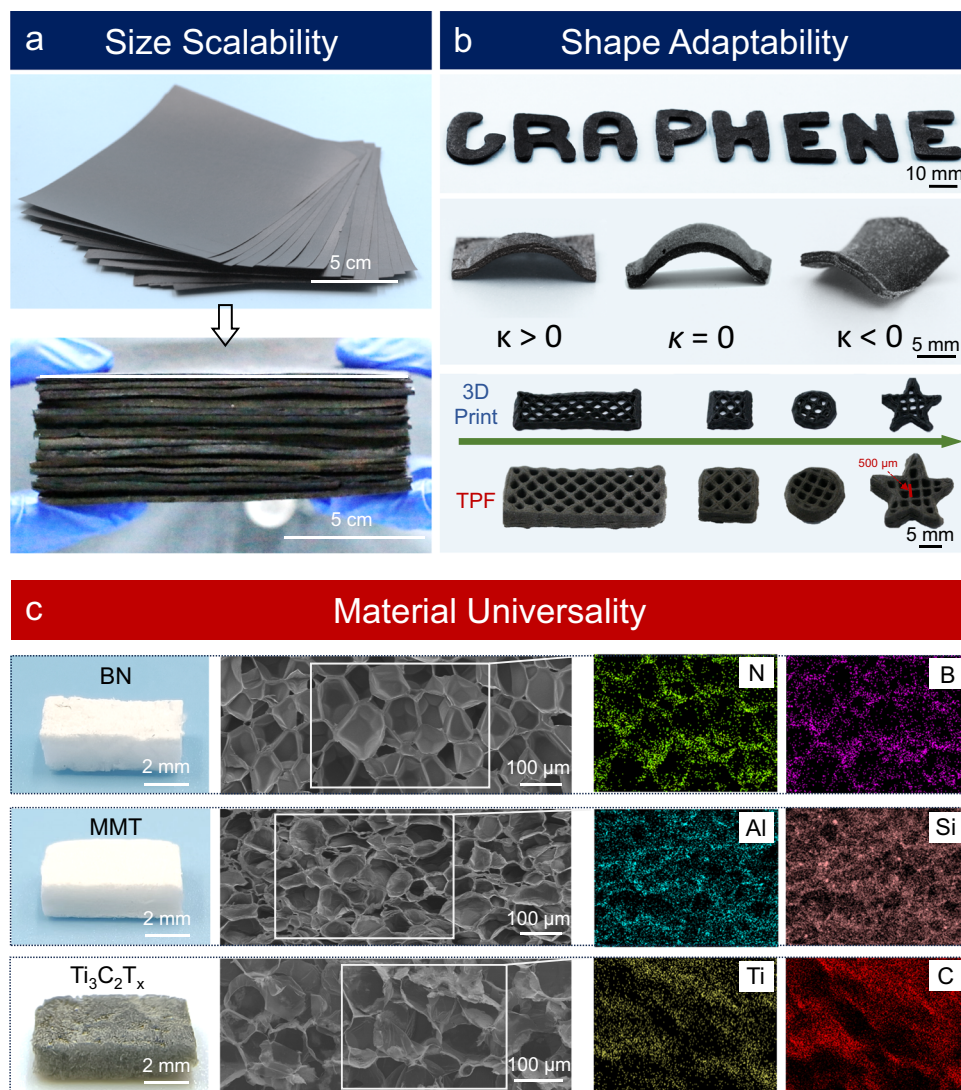


Fig. 5 | Extension of structure and material by TPF method. Digital images showing **a** size scalability and **b** structural adaptability of GMs. **c** Digital images, cross-sectional SEM and energy-dispersive spectrometer images of BN, MMT and $\text{Ti}_3\text{C}_2\text{T}_x$ based monoliths. Source data are provided as a Source Data file.

consecutive heating cycles ($0\text{--}300\text{ }^\circ\text{C}$, $10\text{ }^\circ\text{C min}^{-1}$). The first cycle was used to eliminate the material's thermal history, while the second cycle provided stable thermodynamic data for analysis, with cooling rates maintained at $10\text{ }^\circ\text{C min}^{-1}$ to match the heating rate throughout the process, the peak is the peak melting temperature of PEG. The dynamic mechanical analysis was performed on a DMA 242E (NETZSCH Instruments). The film was cut into strips measuring $15\text{ mm} \times 2\text{ mm}$ (length \times width) and clamped in the DMA fixture. A preload was applied by adjusting the displacement to $15\text{ }\mu\text{m}$ (equivalent to 0.1% strain relative to the initial measured length), ensuring optimal specimen engagement while minimizing interfacial stress concentration at the clamping regions. Testing was conducted under nitrogen atmosphere, with heating from room temperature to $150\text{ }^\circ\text{C}$ at a rate of $2\text{ }^\circ\text{C min}^{-1}$ and a frequency of 1 Hz . Forces were monitored using a high-resolution load cell ($\pm 4\text{ N}$ accuracy), and grip torque was standardized to $0.6\text{ N}\cdot\text{m}$ using a calibrated torque wrench to ensure mechanical consistency. The compressive tests were taken on the Instron Legend 2344 machine. A high-precision Instron® load cell (50 N maximum capacity) was utilized for force measurement. The monolith was cut into a $10\text{ mm} \times 10\text{ mm}$ (length \times width) rectangular sample and compressed to varying strain levels at room temperature, with a loading velocity of 1 mm min^{-1} .

Raman spectra were obtained on Horiba LabRAM HR Evolution. The Raman spectra of graphene include the G peak located at $\sim 1580\text{ cm}^{-1}$ and 2D peak at $\sim 2700\text{ cm}^{-1}$, caused by the in-plane optical vibration (degenerate zone center E_{2g} mode) and second-order zone boundary phonons, respectively. The D peak, located at $\sim 1350\text{ cm}^{-1}$ due to first-order zone boundary phonons, is absent from defect-free graphene, but exists in defected graphene³². The progressive decrease in the I_D/I_G ratio with annealing temperature (Figure. S8a) directly reflects the reduction of defect density. At $1600\text{ }^\circ\text{C}$, the low I_D/I_G value (~ 0.3) indicates the structural restoration of lattice imperfections, such as the removal of residual oxygen groups (e.g., epoxy and hydroxyl) and the recombination of carbon vacancies³³. The 2D peak ($\sim 2700\text{ cm}^{-1}$) is a second-order overtone of the D peak, sensitive to the electronic band structure and interlayer interactions. The spatial uniformity of the monolith's structure is validated by the consistent Raman spectra across ten distinct regions (Figure. S9).

XRD profiles were collected on a X'Pert Pro (PANalytical) diffractometer using monochromatic $\text{Cu } 17\text{ K}\alpha 1$ radiation ($\lambda = 1.5406\text{ \AA}$) at 40 kV . The unannealed GO monolith exhibits a prominent diffraction peak at 2θ of 10.5° , corresponding to the (001) crystallographic plane of oxidized graphene layers. This peak arises from the expanded interlayer spacing ($\sim 0.84\text{ nm}$) caused by oxygen-containing functional

groups (e.g., hydroxyl, epoxy). The broad nature of this peak reflects the disordered stacking of oxidized layers and the presence of amorphous domains, consistent with the structural heterogeneity of GO. Upon thermal annealing, the (001) peak gradually diminishes, and a new peak emerges at 2θ of 26° which is assigned to the (002) plane of graphitic carbon³⁴. The shift to higher angles indicates a reduction in interlayer spacing from 0.84 nm (GO) to 0.34 nm (annealed GM). This transition confirms the effective removal of oxygen functional groups and the restoration of sp^2 -hybridized carbon networks through high-temperature processes^{35,36}. The narrowing of the (002) peak's full width at half maximum (FWHM) with increasing annealing temperature directly correlates with enhanced crystallinity. This trend reflects the growth of sp^2 domains and the reduction of lattice defects³⁷ (Figure S8).

Statistics and reproducibility

All experiments were repeated independently for three times with similar results without specific annotations. The average pore size and pore density were systematically analyzed from two independent samples, with five randomly selected regions (each spanning 0.16 mm^2) analyzed in each sample. The wall thickness was analyzed from two independent samples, with five randomly selected walls measured in each sample. All graphs were plotted and analyzed by the Origin Pro 9, and the size statistics were conducted with Image J 1.54 g.

Reporting summary

Further information on research design is available in the Nature Portfolio Reporting Summary linked to this article.

Data availability

The data generated in this study are provided in the Source Data file. All data that support the findings of this study are available from the corresponding author upon request. Source data are provided with this paper.

References

- Qiu, L., Liu, J. Z., Chang, S. L. Y., Wu, Y. & Li, D. Biomimetic superelastic graphene-based cellular monoliths. *Nat. Commun.* **3**, 1241 (2012).
- Mao, L., et al. Stiffening of graphene oxide films by soft porous sheets. *Nat. Commun.* **10**, 3677 (2019).
- Zhao, Y. et al. A versatile, ultralight, nitrogen-doped graphene framework. *Angew. Chem. Int. Ed.* **51**, 11371–11375 (2012).
- Kong, J. et al. High-mass-loading porous $\text{Ti}_3\text{C}_2\text{T}_x$ films for ultrahigh-rate pseudocapacitors. *ACS Energy Lett.* **5**, 2266–2274 (2020).
- Worsley, M. A. et al. Synthesis of graphene aerogel with high electrical conductivity. *J. Am. Chem. Soc.* **132**, 14067–14069 (2010).
- Li, C., et al. Ultralight covalent organic framework/graphene aerogels with hierarchical porosity. *Nat. Commun.* **11**, 4712 (2020).
- Wu, M., et al. Superelastic graphene aerogel-based metamaterials. *Nat. Commun.* **13**, 4561 (2022).
- Yang, G. et al. Ultra-stretchable graphene aerogels at ultralow temperatures. *Mater. Horiz.* **10**, 1865–1874 (2023).
- Liu, P. et al. 3D lamellar-structured graphene aerogels for thermal interface composites with high through-plane thermal conductivity and fracture toughness. *Nano-Micro Lett.* **13**, 22 (2020).
- Ma, J., et al. Synthesis of superelastic, highly conductive graphene aerogel/liquid metal foam and its piezoresistive application. *Chemistry* **30**, e2023035 (2024).
- Liu, X. et al. Hyperbolic graphene framework with optimum efficiency for conductive composites. *ACS Nano* **16**, 14703–14712 (2022).
- Mecklenburg, M. et al. Aerographite: Ultra lightweight, flexible nanowall, carbon microtube material with outstanding mechanical performance. *Adv. Mater.* **24**, 3486–3490 (2012).
- Seraji, S. M., Jin, X., Yi, Z., Feng, C. & Salim, N. V. Ultralight porous poly (vinylidene fluoride)-graphene nanocomposites with compressive sensing properties. *Nano Res* **14**, 2620–2629 (2021).
- Liu, W. et al. Fabrication of ultralight three-dimensional graphene networks with strong electromagnetic wave absorption properties. *J. Mater. Chem. A* **3**, 3739–3747 (2015).
- Li, C. et al. Superelastic and arbitrary-shaped graphene aerogels with sacrificial skeleton of melamine foam for varied applications. *Adv. Funct. Mater.* **28**, 1704674 (2017).
- Cao, M. et al. Vertical array of graphite oxide liquid crystal by microwire shearing for highly thermally conductive composites. *Adv. Mater.* **35**, 2300077 (2023).
- Ghidiu, M., Lukatskaya, M. R., Zhao, M. Q., Gogotsi, Y. & Barsoum, M. W. Conductive two-dimensional titanium carbide 'clay' with high volumetric capacitance. *Nature* **516**, 78–81 (2014).
- Xu, Y. X., Sheng, K. X., Li, C. & Shi, G. Q. Self-assembled graphene hydrogel via a one-step hydrothermal process. *ACS Nano* **4**, 4324–4330 (2010).
- Li, M., et al. Preferential ice growth on grooved surface for crisscross-aligned graphene aerogel with large negative Poisson's ratio. *Nat. Commun.* **14**, 7855 (2023).
- Zhang, Q. et al. Hyperbolically patterned 3D graphene metamaterial with negative Poisson's ratio and superelasticity. *Adv. Mater.* **28**, 2229–2237 (2016).
- Yang, H. et al. Superplastic air-dryable graphene hydrogels for wet-press assembly of ultrastrong superelastic aerogels with infinite macroscale. *Adv. Funct. Mater.* **29**, 1901917 (2019).
- Yang, H. et al. Retarding ostwald ripening to directly cast 3D porous graphene oxide bulks at open ambient conditions. *ACS Nano* **14**, 6249–6257 (2020).
- Lv, L., Zhang, P., Xu, T. & Qu, L. Ultrasensitive pressure sensor based on an ultralight sparkling graphene block. *ACS Appl. Mater. Interfaces* **9**, 22885–22892 (2017).
- Lee, S. T. & Park, C. B. *Foam Extrusion* (CRC Press, 2014).
- Kim, T., Jung, G., Yoo, S., Suh, K. S. & Ruoff, R. S. Activated graphene-based carbons as supercapacitor electrodes with macro- and mesopores. *ACS Nano* **7**, 6899–6905 (2013).
- Chu, Z. et al. Fabrication of porous SiC (core)/C (shell) fibres using a hybrid precursor of polycarbosilane and pitch. *Carbon* **48**, 2115–2118 (2010).
- Li, P., et al. Continuous crystalline graphene papers with gigapascal strength by intercalation modulated plasticization. *Nat. Commun.* **11**, 2645 (2020).
- Li, P. et al. Highly crystalline graphene fibers with superior strength and conductivities by plasticization spinning. *Adv. Funct. Mater.* **30**, 2006584 (2020).
- Guo, F. et al. Hydroplastic micromolding of 2D sheets. *Adv. Mater.* **33**, 2008116 (2021).
- Pang, K. et al. Hydroplastic foaming of graphene aerogels and artificially intelligent tactile sensors. *Sci. Adv.* **6**, eabd4045 (2020).
- Wilson, A. J. *Foams: Physics, Chemistry and Structure* (Springer, 1989).
- Lucchese, M. M. et al. Quantifying ion-induced defects and Raman relaxation length in graphene. *Carbon* **48**, 1592–1597 (2010).
- Tuinstra, F. & Koenig, J. L. Raman spectrum of graphite. *J. Chem. Phys.* **53**, 1126–1130 (1970).
- Trucano, P. & Chen, R. Structure of graphite by neutron diffraction. *Nature* **258**, 136–137 (1975).
- Krishnamoorthy, K., Veerapandian, M., Yun, K. & Kim, S. J. The chemical and structural analysis of graphene oxide with different degrees of oxidation. *Carbon* **53**, 38–49 (2013).
- Lerf, A., He, H., Forster, M. & Klinowski, J. Structure of graphite oxide revisited. *J. Phys. Chem. B* **102**, 4477–4482 (1998).

37. Huang, H. H., De Silva, K. K. H., Kumara, G. R. A. & Yoshimura, M. Structural evolution of hydrothermally derived reduced graphene oxide. *Sci. Rep.* **8**, 6849 (2018).
38. Napolitano, S., Glynos, E. & Tito, N. B. Glass transition of polymers in bulk, confined geometries, and near interfaces. *Rep. Prog. Phys.* **80**, 036602 (2017).
39. Zhao, C. et al. Layered nanocomposites by shear-flow-induced alignment of nanosheets. *Nature* **580**, 210–215 (2020).
40. Zhu, C., et al. Highly compressible 3D periodic graphene aerogel microlattices. *Nat. Commun.* **6**, 6962 (2015).
41. Yang, M. et al. Biomimetic architected graphene aerogel with exceptional strength and resilience. *ACS Nano* **11**, 6817–6824 (2017).
42. Wang, C. et al. Freeze-casting produces a graphene oxide aerogel with a radial and centrosymmetric structure. *ACS Nano* **12**, 5816–5825 (2018).
43. Hu, H., Zhao, Z., Wan, W., Gogotsi, Y. & Qiu, J. Ultralight and highly compressible graphene aerogels. *Adv. Mater.* **25**, 2219–2223 (2013).
44. Wu, Y., et al. Three-dimensionally bonded spongy graphene material with super compressive elasticity and near-zero Poisson's ratio. *Nat. Commun.* **6**, 6141 (2015).
45. Gao, H. L., et al. Super-elastic and fatigue resistant carbon material with lamellar multi-arch microstructure. *Nat. Commun.* **7**, 12920 (2016).
46. Zhao, X., Yao, W., Gao, W., Chen, H. & Gao, C. Wet-spun superelastic graphene aerogel millispheres with group effect. *Adv. Mater.* **29**, 1701482 (2017).
47. Barg, S., et al. Mesoscale assembly of chemically modified graphene into complex cellular networks. *Nat. Commun.* **5**, 4328 (2014).
48. Yang, H. et al. Reconstruction of inherent graphene oxide liquid crystals for large-scale fabrication of structure-intact graphene aerogel bulk toward practical applications. *ACS Nano* **12**, 11407–11416 (2018).
49. Li, G., Dong, D., Hong, G., Yan, L., Zhang, X. & Song, W. High-efficiency cryo-thermocells assembled with anisotropic holey graphene aerogel electrodes and a eutectic redox electrolyte. *Adv. Mater.* **31**, 1901403 (2019).
50. Chen, Y., et al. Environment-adaptive, anti-fatigue thermal interface graphene foam. *Carbon* **212**, 118142 (2023).
51. Li, Z. et al. Precise Thermoplastic processing of graphene oxide layered solid by polymer intercalation. *Nano-Micro Lett.* **14**, 12 (2022).
52. Cheng, Y., et al. Enhanced mechanical, thermal, and electric properties of graphene aerogels via supercritical ethanol drying and high-temperature thermal reduction. *Sci. Rep.* **7**, 1439 (2017).

Acknowledgements

We thank N. Zheng at State Key Laboratory of Chemical Engineering in Zhejiang University for performing SEM analysis. This work is supported by National Key Research and Development Program of China (2022YFA1205300, 2022YFA1205301 to Z.X.), National Natural Science Foundation of China (52090031, 52090030 to C.G., 52272046 to Y.L.), Hundred Talents Program of Zhejiang University (188020*194231701/

113112300+1944223R3/003, 112300+1944223R3/004 to Y.L.), Fundamental Research Funds for the Central Universities (226-2024-00074 to Z.X., 226-2024-00172 to C.G.), Shanxi-Zheda Institute of New Materials and Chemical Engineering (2022SZ-TD011 to C.G., 2022SZ-TD012 to Z.X.).

Author contributions

K.P., Z.X. and Z.L. conceived the project. Z.L. and X.L. wrote the manuscript. K.P., Z.X., Y.L. and C.G. contributed to the literature review. Z.L., X.L. and K.P. analyzed the data. K.L. helped in in-situ SEM tests. Y.G. performed EDS test. C.Z., J.L. and X.L. conducted thermal conductivity measurements. Z.L. and X.L. led the experiment with support from K.P. and Z.X. All authors discussed the results and commented on the manuscript.

Competing interests

The authors declare no competing interests.

Additional information

Supplementary information The online version contains supplementary material available at <https://doi.org/10.1038/s41467-025-61123-3>.

Correspondence and requests for materials should be addressed to Kai Pang, Zhen Xu or Chao Gao.

Peer review information *Nature Communications* thanks Ernesto Di Maio and the other, anonymous, reviewer(s) for their contribution to the peer review of this work. A peer review file is available.

Reprints and permissions information is available at <http://www.nature.com/reprints>

Publisher's note Springer Nature remains neutral with regard to jurisdictional claims in published maps and institutional affiliations.

Open Access This article is licensed under a Creative Commons Attribution-NonCommercial-NoDerivatives 4.0 International License, which permits any non-commercial use, sharing, distribution and reproduction in any medium or format, as long as you give appropriate credit to the original author(s) and the source, provide a link to the Creative Commons licence, and indicate if you modified the licensed material. You do not have permission under this licence to share adapted material derived from this article or parts of it. The images or other third party material in this article are included in the article's Creative Commons licence, unless indicated otherwise in a credit line to the material. If material is not included in the article's Creative Commons licence and your intended use is not permitted by statutory regulation or exceeds the permitted use, you will need to obtain permission directly from the copyright holder. To view a copy of this licence, visit <http://creativecommons.org/licenses/by-nc-nd/4.0/>.

© The Author(s) 2025